Electronic Supplementary Material (ESI) for Materials Advances.

Supporting Information

Mesoporous zinc platinate and platinum nanotubes: Insights to formation mechanism and their catalytic activity

Shwetha Shetty[1], Ankita Mathur[2,] Neha Sakhuja[3], Dipanwita Chatterjee[1], Subhajit Kundu[1], Aditi Halder[4], Navakanta Bhat[3], and N. Ravishankar[1]*

1. *Materials Research Centre, Indian Institute of Science, Bangalore- 560012, India.*

†Presently at Department of Chemistry, University of Helsinki, A.I.Virtasen aukio 1, Helsinki – 00014, Finland

2. *School of Engineering, IIT-Mandi, Kamand, Himachal Pradesh-175005, India*

3. *Centre for Nanoscience and Engineering, Indian Institute of Science, Bangalore-560012, India*

4. *School of Basic Sciences, IIT-Mandi, Kamand, Himachal Pradesh-175005, India*

*Corresponding author, Email: nravi@iisc.ac.in

Electrochemical Measurements

Electrochemical measurements for methanol oxidation reaction are carried out in a conventional 3-electrode electrochemical setup connected to a potentiostat (Model PG-16250, Techno Science Instruments, Bangalore). Platinum foil is used as a counter electrode and a saturated Ag/AgCl electrode served as a reference electrode. About 3 mg of freshly synthesized porous nanotube sample is dispersed by sonication in 1 mL isopropanol solution mixed with 20 uL of 5% w/w Nafion solution (Alfa Aesar) to get a homogeneous slurry. This catalyst ink is drop cast on Toray carbon paper electrode with a fixed geometric area of 0.5 cm^2 and air-dried. The same procedure is followed to prepare the catalyst ink of commercial Pt/C (40%). Electrochemical surface area (ECSA) is obtained from cyclic voltammetry (CV) scans performed at a scan rate of 40 mV/s in an Ar saturated 0.5 M KOH solution bath. An initial set of 10 cycles is performed prior to getting reproducible CV data for all the samples. ECSA is calculated by the standard procedure of integrating the area under the anodic desorption peak for the under potential deposited hydrogen after double layer charge correction (QH in cm^2). Specific ECSA is calculated using the formula QH/(0.21xMPt) where M_{Pt} is the loading of the active metal Pt in the porous nanotubes and 0.21 is the charge due to the complete oxidation of a monolayer of adsorbed hydrogen on pure Pt surface (in mC/cm^2). CO-stripping voltammetry is performed in 0.5 M KOH solution at a scan rate of 10 mV/s. Initially, Ar is used to deoxygenate the electrolyte solution for 15 min. Later, CO is continuously bubbled at a potential bias of 0.1 V vs RHE for 15 min followed by Ar for 15 min to remove dissolved CO from the electrolyte. A potential sweep is commenced at 0.1 V at a scan rate of 10 mV/s to collect the first stripping cycle.

Oxygen reduction reaction (ORR) measurements are done on Autolab electrochemical workstation (Metrohm) at room temperature in a three-electrode system using 0.1 M KOH as electrolyte. A rotating glassy carbon disc electrode (RDE) with a diameter of 5 mm, was used as a working electrode, Ag/AgCl (in 3 M KCl) as a reference electrode, and platinum wire as the counter electrode. Ink for analysis was prepared by adding 2 mg pPt-NTs powder and 8 mg Vulcan carbon in 990 µl IPA: distilled water (1:1 v/v ratio) and 10 µl Nafion solution (5 wt%). The ink was sonicated for 45 minutes prior to drop cast 7 µl (loading = 0.11 mg/cm^2) over the working electrode. To evaluate their electrocatalytic ability, cyclic voltammetry (CV) and linear sweep voltammetry (LSV) studies were carried out in 0.1 M KOH electrolyte solution. To evaluate ORR, rotating ring disk electrode (RRDE) measurements are done on Pine Instruments setup connected to Autolab bi-potentiostat. Electrochemical Impedance Spectroscopy (EIS) is performed in the frequency range of 0.1 Hz to 100 kHz and potential bias of 10 mV amplitude.

Sensing studies

The gas sensing studies are performed in a custom-constructed volumetric gas chamber connected to mass flow controllers (Alicat), SMU (Keithley 2450), and temperature controller (Eurotherm) as discussed in our previous works1. In brief, the controlled flow of gases is purged onto the sensor using MFC's and the total flow was fixed at 500 sccm. Dry air is used as a reference and diluent gas to achieve the desired concentrations of SO2. The sensor is probed at

5V using SMU and the dynamic current values are recorded in the presence/absence of target gas (SO_2) at different temperatures. The schematic of the set-up is shown in Fig. S14.

Characterization techniques

Powder X-ray diffraction date is collected using PANalytical X'pert PRO XRD system with Cu-Kα (1.54060 Å) radiation generated at 30 mA and 40 kV at a step size of 0.01° (2θ) per second. Field emission SEM images are captured using Ziess Ultra 55 field emission SEM. Bright field and high-resolution TEM images are recorded using Tecnai T20 TEM operated at 200 kV FEI-Titan operated at 300 kV equipped with CEOS probe corrector is used to collect HAADF-STEM images. STEM-EDX spectroscopy analysis is performed in the same instrument. TEM samples are prepared on a carbon coated copper grid by drop casting a dilute solution of the sample in acetone and drying in vacuum prior to analysis. Kratos Analytical Axis Ultra XPS instrument is used for XPS analysis using Al Kα (1486.6 eV) monochromatic source for excitation. Sample powder is dusted onto a conducting carbon tape. Binding energy shifts in high resolution elemental scans due to charge accumulation are corrected using adventitious C1s at 284.6 eV. The analysis of data is done in XPSPEAK4.1 software. Diffuse reflectance spectra are collected using Perkin Elmer Lambda 750 spectrophotometer fitted with integrating sphere (60 mm, Labsphere) in the reflection mode. %R values are converted to Kubelka-Munk absorption function F(R) which is applied to Tauc plot of $\{h\nu F(R)\}^{1/r}$ vs hν (where r = ½ for direct allowed transitions and r = 2 for indirect allowed transition) to get the bandgap values. BET adsorption-desorption isotherms at 77 K, surface area measurements and pore volume estimation are obtained from Anton Paar Quantachrome Autosorb iQ TPx instrument. ICP-MS chemical composition analysis is performed using Thermo X series quadrupole instrument.

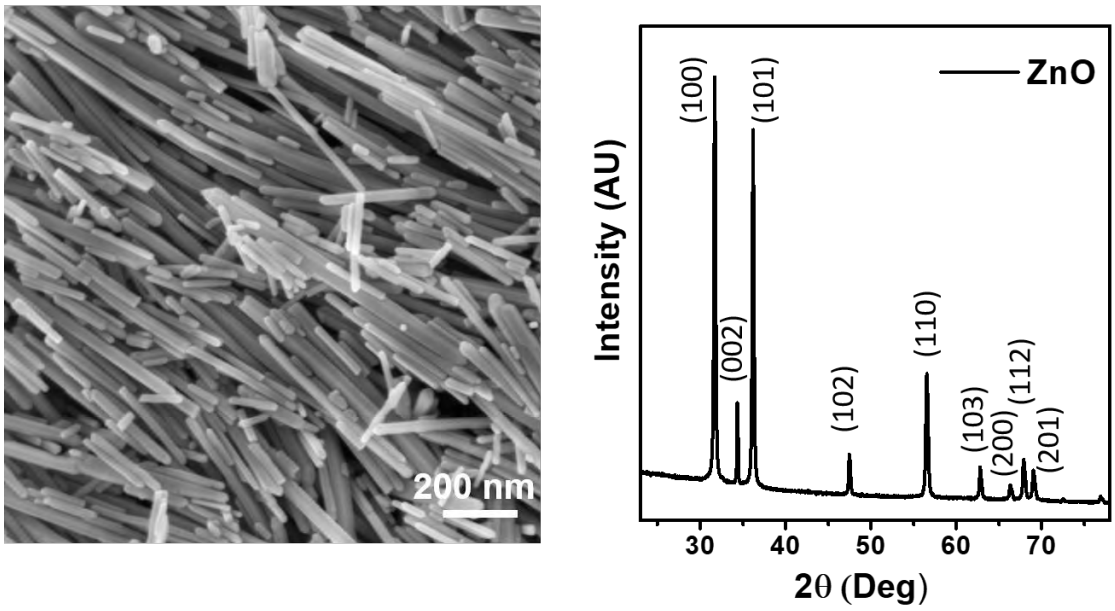

Fig. S1: SEM and powder X-ray diffraction data of the freshly synthesized ZnO nanorods. Peaks are indexed to Wurtzite crystal structure (ICDD-00-036-1451)

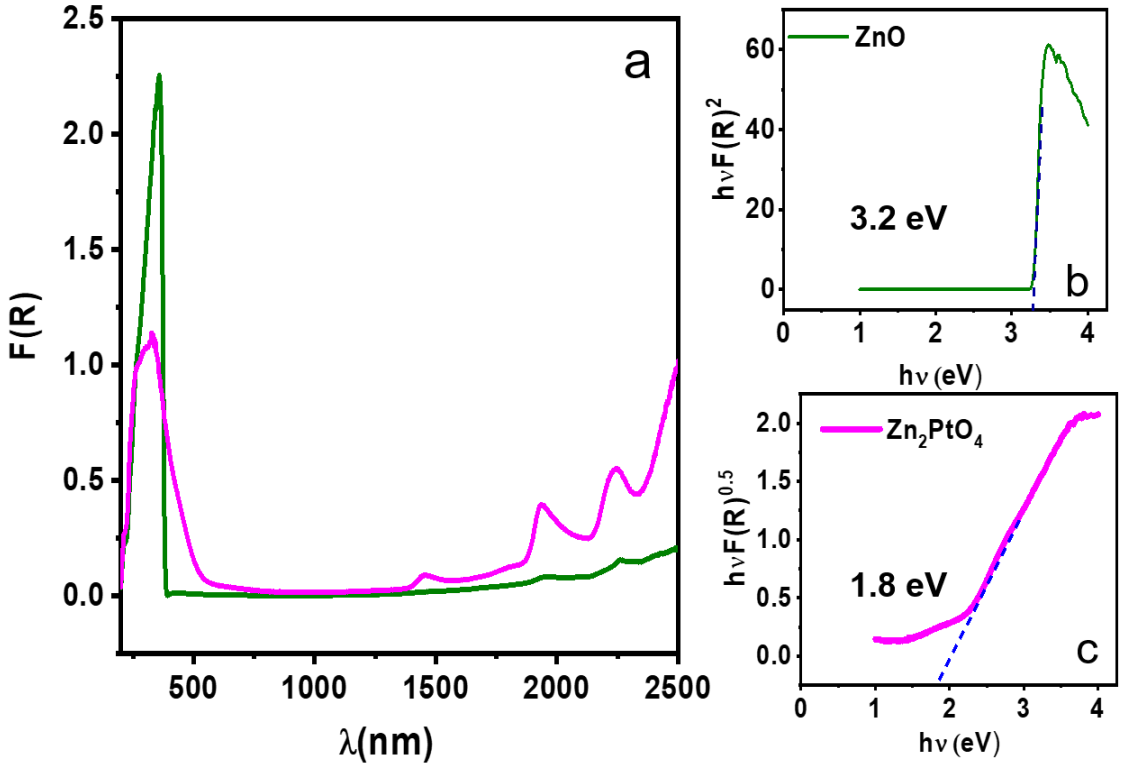

Fig. S2: (a) UV-Vis DRS studies on intermediate phase porous nanotubes (purple) and ZnO nanorods (green). (b) Direct band gap Tauc plot for ZnO nanorods (c) Indirect band gap Tauc plot for Zn_2PtO_4 phase.

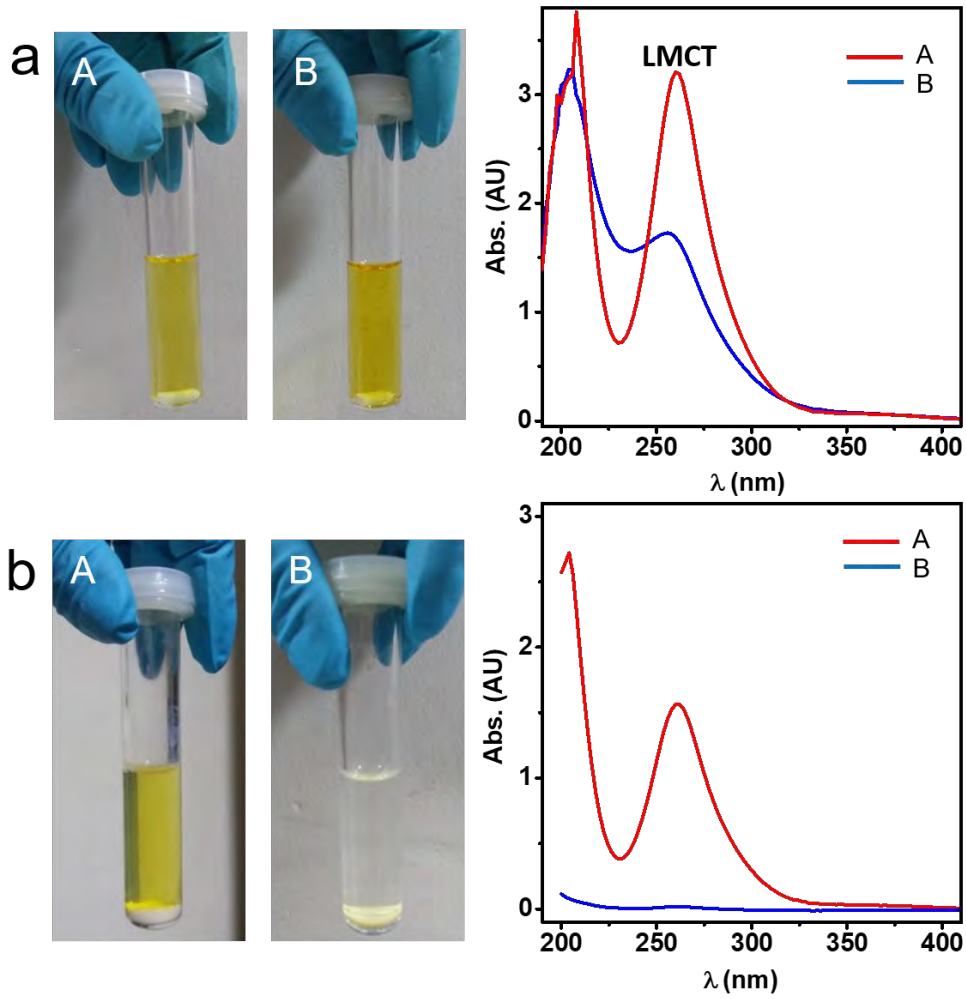

Fig. S3: (a) Snapshots of aqueous H_2PtCl_6 solution (0.012M) in a microwave reaction vessel (A) before and (B) after microwave reaction in the absence of template ZnO nanorods. Corresponding UV-Vis spectra for these samples is shown on the right side. The peak at 262 nm corresponds to electronic transition due to ligand to metal charge transfer (LMCT) in $[PtCl_6]^{2-}$. (b) Snapshots of aqueous mixture of H_2PtCl_6 (0.012M) and ZnO nanorods in a microwave reaction vessel (A) before and (B) after microwave reaction. Corresponding UV-Vis spectra for these samples are shown on the right side. The LMCT peak is suppressed for the supernatant solution in B showing the absence of Pt precursor.

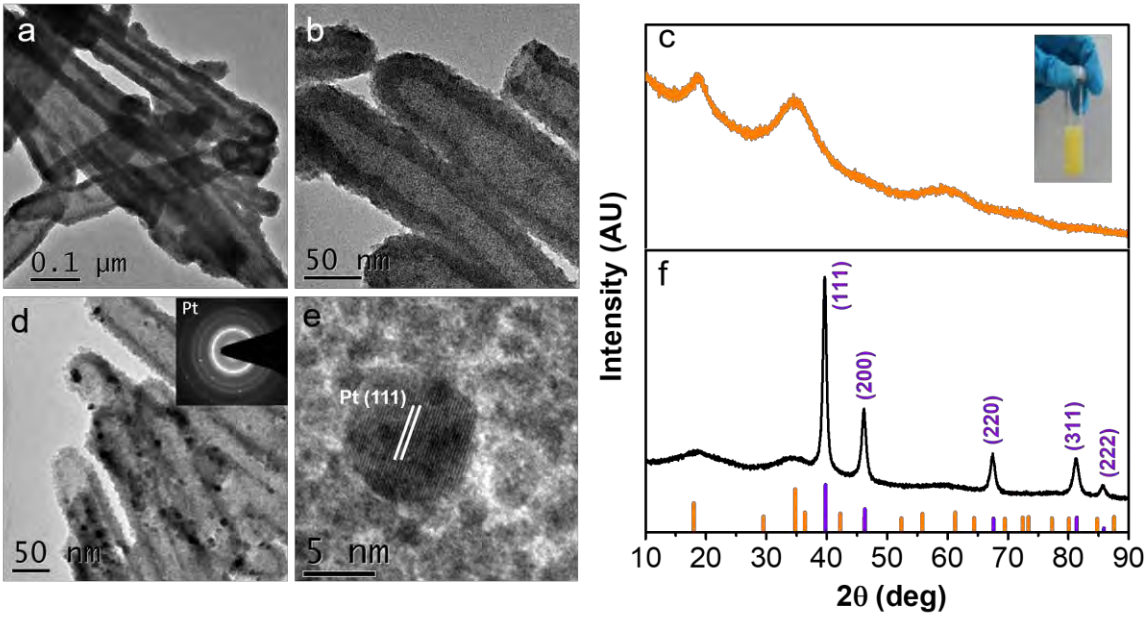

Fig.S4: (a) & (b) BF-TEM images of pZPO-NTs synthesized by microwave reaction time of 1 hour. XRD data of the sample is shown in (c). Inset shows the digital photograph of the product zinc platinate phase formed after 1-hour microwave reaction. (d) BF-TEM images of the pZPO-NTs re-dispersed in water and exposed to microwave irradiation at 200°C showing that the zinc platinate phase is reduced porous Pt nanotubes. Inset shows the FCC diffraction rings which can be indexed to Pt phase (e) HR-TEM image of the larger Pt nanoparticle formed due to the coarsening of the finer crystallites. FCC (111) planes for Pt can be resolved. (f) XRD data of the sample showing intense peaks for FCC platinum phase. Orange lines – ICDD standard Zn_2PtO_4 file 00-023-1499, violet lines – ICDD standard Pt file 00-001-1190.

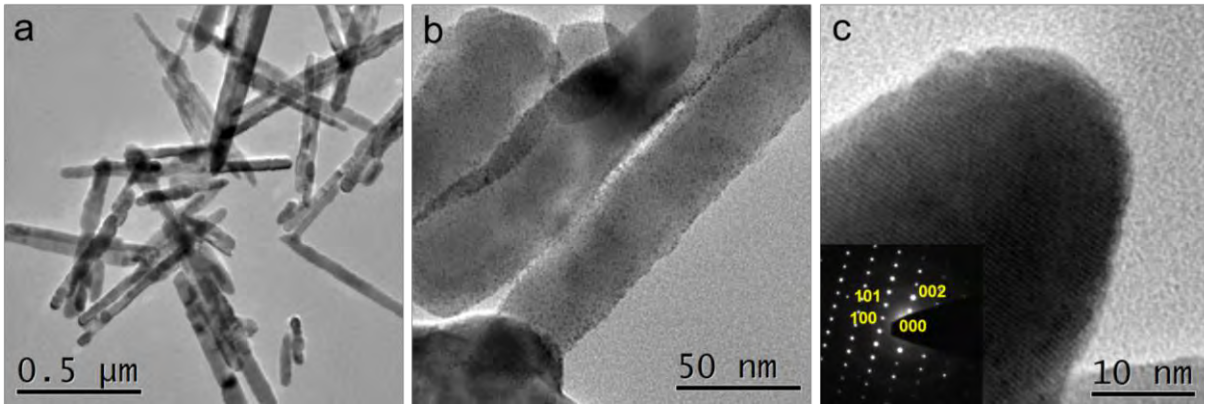

Fig. S5: (a) & (b) BF-TEM images showing that ZnO nanorods are intact after the microwave reaction at 100°C and the nucleation of tiny clusters on the surface of nanorods upon exposure to electron beam. (c) High magnification TEM image from a single ZnO nanorod. Inset shows the diffraction pattern from this nanorod showing that the nanorod has maintained its crystallinity. Broad rings are visible which match with interplanar spacing of platinum.

Scheme 1: Sacrificial template assisted hydrolysis (STAH) mechanism for the formation of porous zinc platinate nanotubes

Step 1 : Dissociation of H_2PtCl_6

$$H_2PtCl_6 \longrightarrow 2H^+ + [PtCl_6]^{2-}$$

Step 2 : Hydrolysis of Pt complex ion

$$2H^+ + [PtCl_6]^{2-} + 2H_2O \longrightarrow [PtCl_4(H_2O)_2]^0 + 2HCl$$

Step 3 : Dissolution of ZnO

$$ZnO + 2HCl \longrightarrow ZnCl_2 + H_2O$$

Sacrificial template accelerated hydrolysis (STAH)

Step 4 : Synthesis of Zn_2PtO_4

$$[PtCl_4(H_2O)_2]^0 + 4ZnO \longrightarrow Zn_2PtO_4 + 2ZnCl_2 + 2H_2O$$

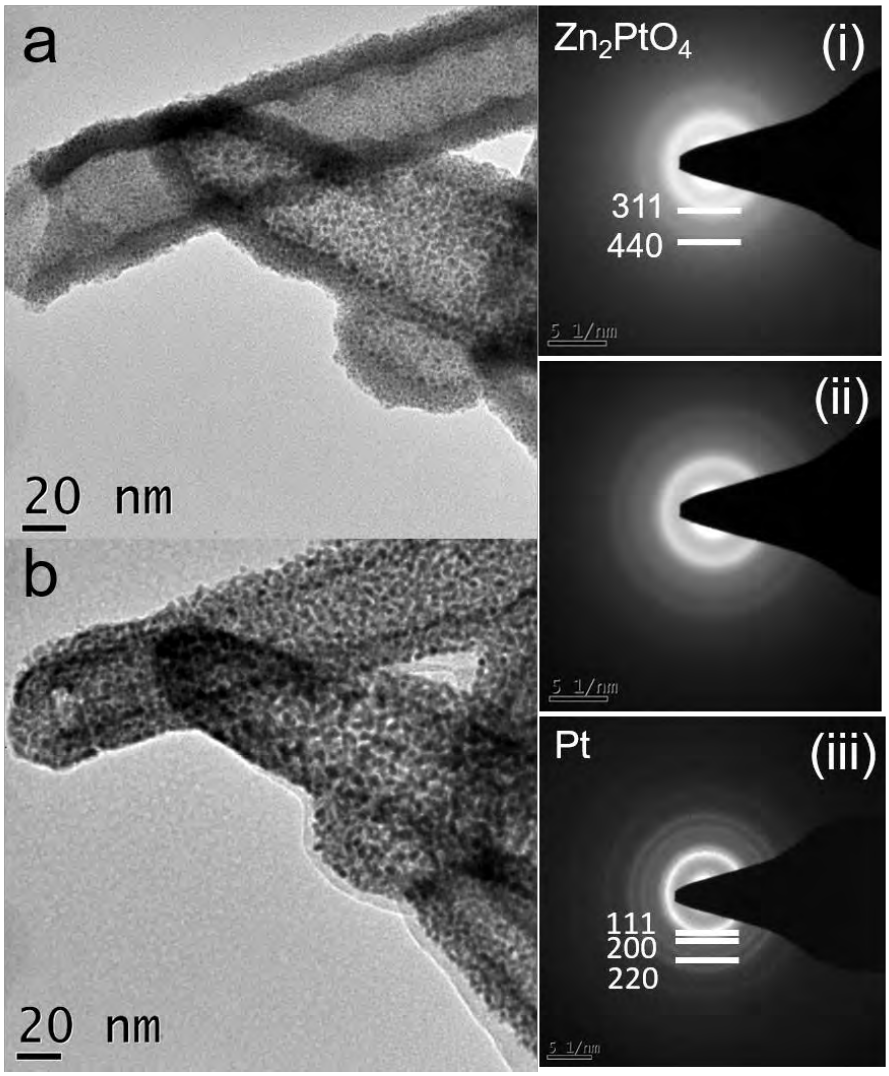

Fig. S6: BF-TEM image of (a) pZPO-NTs. (b) porous Pt nanotube formation upon exposure to electron beam. Side panel from (i) to (iii) shows the corresponding transformation in diffraction patterns from zinc platinate (Zn_2PtO_4) phase to Pt phase. In (i) the diffraction rings can be indexed to 311 and 440 planes of zinc platinate phase. Intense FCC ring pattern is seen in (iii) with the exposure to electron beam which is the Pt phase.

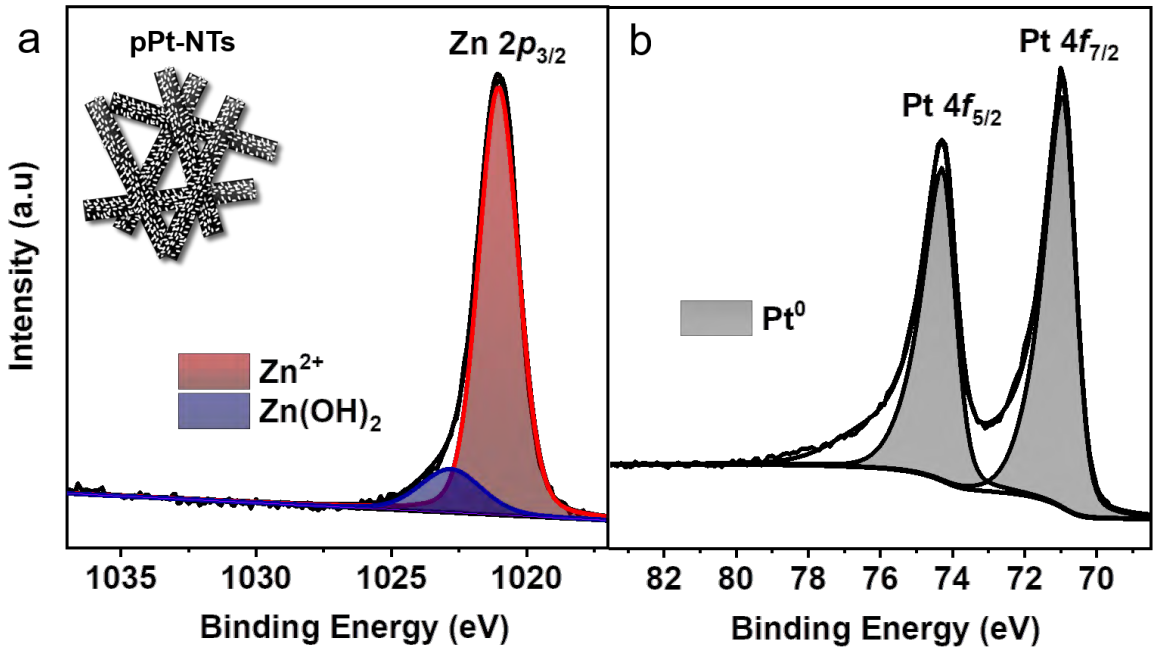

Fig. S7: Core level elemental XPS scans from (a) Zn 2p 3/2 and (b) Pt 4f from porous Pt nanotube sample. Zn exists in +2 oxidation state and Pt exists in metallic state. Traces of $Zn(OH)_2$ is found on the surface of the nanotubes.

Table 1: The relative atom percentages of Zn and Pt obtained by multiple elemental analysis techniques such as XPS, ICP-MS, and STEM-EDS for as synthesized and post catalysis samples of pZPO-NTs, pPt-NTs and acid treated pPt-NTs.

Sample	From XPS (at%)		From ICP (at%)		From STEM-EDS (at%)		From XPS (at%) (Post catalysis)	
	Zn	Pt	Zn	Pt	Zn	Pt	Zn	Pt
pZPO-NTs	68	32	72	28	38	62	15	85
pPt-NTs	42	58	75	25	32	68	10	90
pPt-NTs-E	-	-	46	54	13	87	-	-

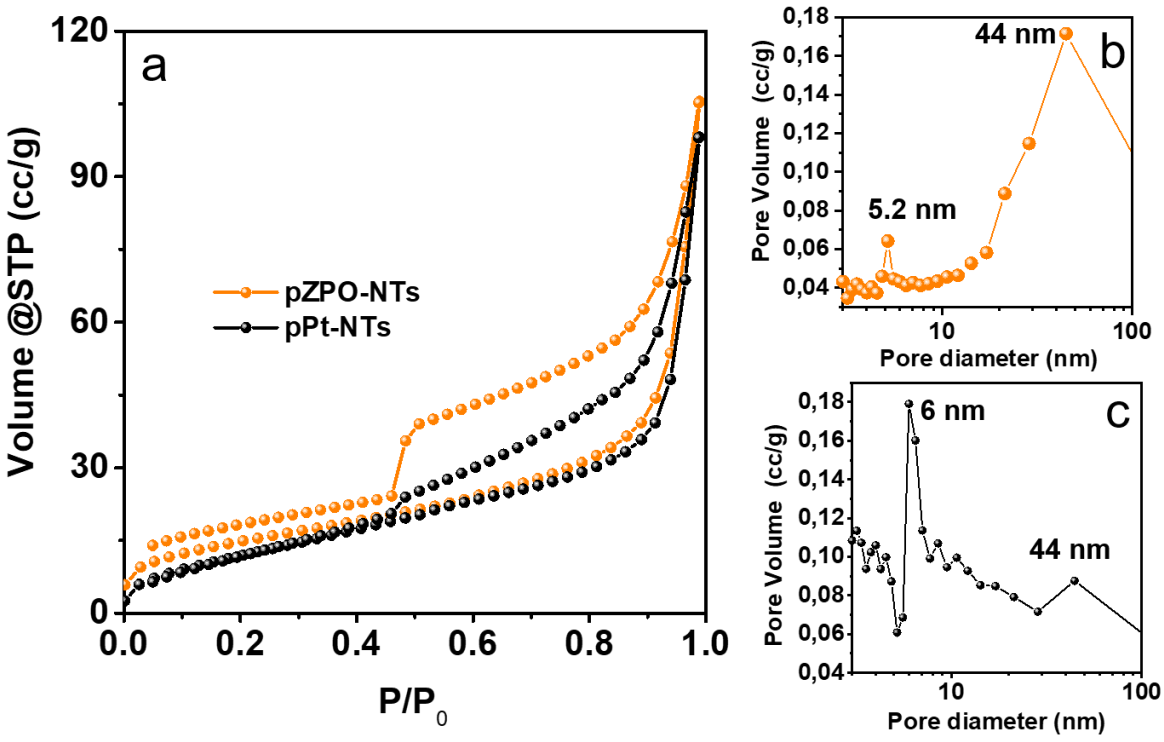

Fig. S8: (a) Nitrogen adsorption desorption isotherms for pZPO-NTs (orange) and porous pPt NTs samples (black). BJH pore size distribution plots for (b) pZPO-NTs and (c) pPt-NTs sample.

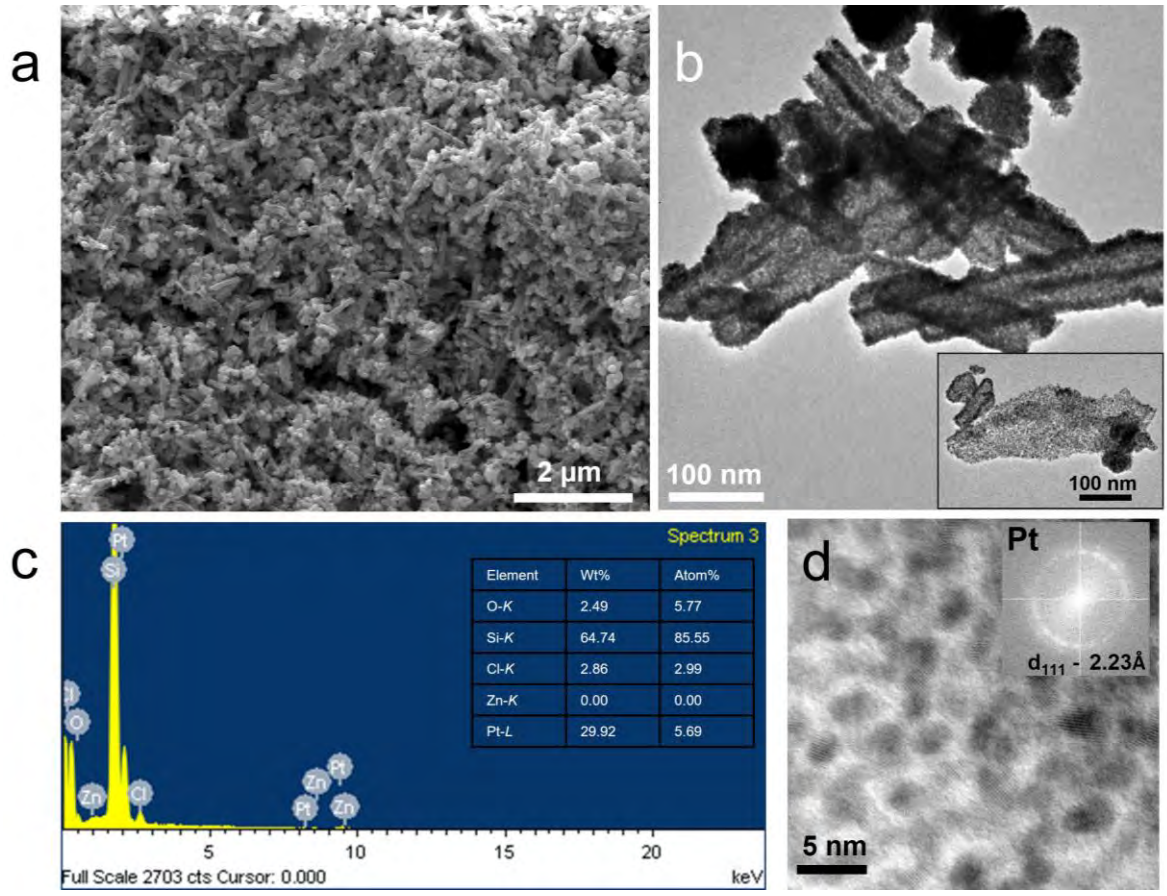

Fig. S9: (a) & (b) SEM and BF-TEM images of the pPt-NTs sample post-treatment with dilute HCl solution. Inset in (b) shows that some of the tubes are damaged losing the tubular structure post-acid treatment. (c) SEM-EDS area scan taken from HCl treated porous Pt sample drop coated on Si substrate. Zn-K (8.6 keV) and Zn-L (1.0 keV) lines are undetected to the sensitivity of the measurement. The inset table shows the weight% and atomic % of the elements detected from the sample. (d) HR-TEM image from the sample shows Pt crystallites of size ~ 3 nm and the FFT (inset) confirms the Pt phase.

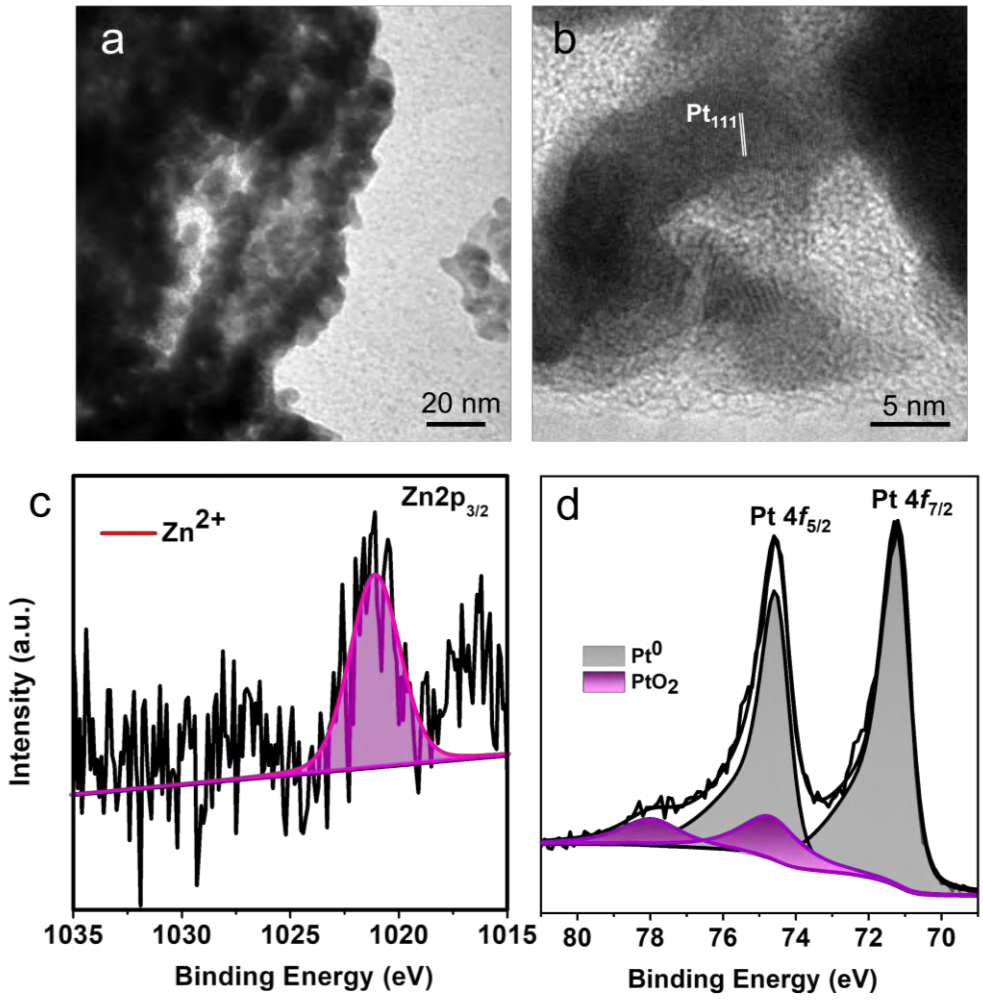

Fig. S10: (a) & (b) BF-TEM images of the pPt-NTs sample post electrocatalysis shows contiguous ligaments which are crystalline. Core level XPS spectra for (c) Zn 2p3/2 and (d) Pt 4f. Intensity of Zn peak is drastically reduced suggesting the dissolution of Zn during MOR cycles. XPS spectra for Pt shows the presence of metallic Pt and Pt in +4 oxidation state.

Oxygen reduction reaction (ORR) studies on porous Pt nanotubes:

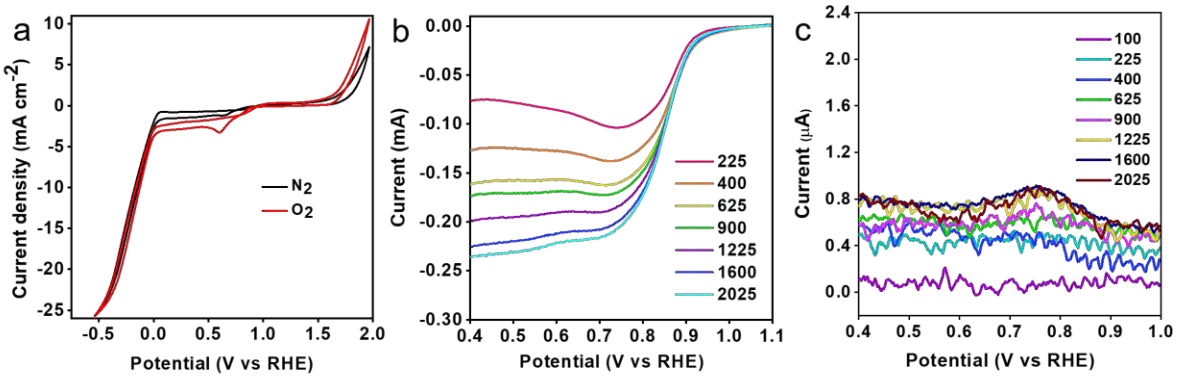

Fig. S11: (a) CV cycles for pPt-NTs and commercial Pt/C in 0.1 M KOH solution at a scan rate of 10 mV/S (b) Polarization plot at different RPMs of the RRDE showing ORR performance of pPt-NTs. (c) LSV plots of ring current at different RPMs to evaluate the amount H_2O_2 formation.

Porous Pt nanotubes (pPt-NTs) are studied for evaluating their electrocatalytic activity towards ORR in 0.1 M KOH medium. The cyclic voltammetry (CV) studies on pPt-NTs are performed by applying potential from 2 V to -0.5 V (vs RHE) at a scan rate of 20 mV/s, initially in nitrogen atmosphere, followed by oxygen saturated atmosphere. To further evaluate their ORR ability, linear sweep voltammetry (LSV) studies using rotating ring disk electrode (RRDE) are performed by applying a potential sweep from 1 V to 0.4 V (vs RHE), at a scan rate of 10 mV/s, in oxygen saturated 0.1 M KOH solution at different RPMs. The ring potential was kept at 0.4 V. The mechanistic pathway for reduction of oxygen by RRDE, is deduced from calculating the percentage formation of intermediate H_2O_2 and the number of electrons transferred during the reaction (n) using the following equations.

$$\% H_2O_2 = 2 \times [I_R/N] / [I_D + I_R/N] \times 100\% \quad (1)$$

$$n = 4I_D / [I_D + I_R/N] \quad (2)$$

where I_R, I_D and N are the faradaic current at ring, faradaic current at disk and collection efficiency (N = 0.37 for Au ring) respectively.

To study the kinetics of ORR by pPt-NTs, Koutecky- Levich (K-L) plot was drawn following K-L equation,

$$1/I = 1/I_k + 1/I_{Lev} \quad (3)$$

where, I is the disk current density, I_k is the kinetic current density and I_{Lev} is the Levich current density. I_k and I_{Lev} are calculated as follows,

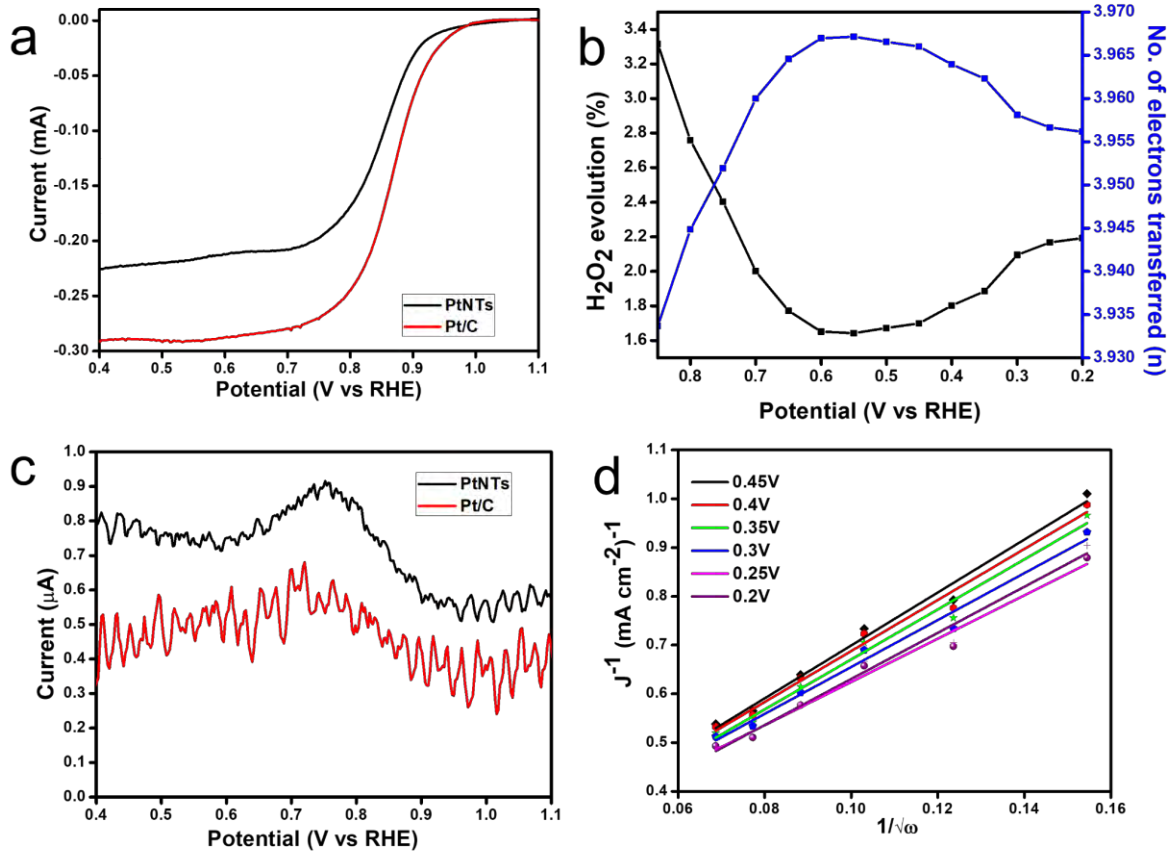

Fig. S12: (a) LSV curve for pPt-NTs and Pt/C in 0.1 M KOH solution at a scan rate of 10 mV/S at 1600 rpm (b) Percentage of H_2O_2 evolution and the number of electrons transferred during the oxygen reduction reaction (c) RRDE studies at a ring potential of 0.4 V at 1600 rpm to study the H_2O_2 evolution current. (d) K-L plots calculated from RRDE studies.

$$I_k = nFAk_{O_2}C_{O_2}\Gamma_{catalyst} \quad (4)$$

$$I_{Lev} = 0.62nFAC_{O_2}D_{O_2}^{2/3}\, v^{-1/6}\omega^{1/2} \quad (5)$$

where n is the number of overall electron transfer in the oxygen reduction reaction, F is the Faraday constant (96485 C/mol), k_{O_2} is the rate constant for ORR (m/s), A is the area of electrode (0.125 cm^2), C_{O_2} is the concentration of dissolved oxygen (1.21 mol/m^3 in 0.1 M KOH) and $\Gamma_{catalyst}$ is the surface concentration of the catalysts (0.1 mg/cm^2). D_{O_2} is the diffusion coefficient of O_2 in solution (1.87 × 10−9 m^2/s in 0.1 M KOH), v is the kinematic viscosity (1 × 10^{-6} m^2/s in 0.1 M KOH) and ω is the angular frequency of rotation (rad/s).

The cyclic voltammetry studies (Fig. S11a) show that pPt-NTs have both hydrogen evolution and oxygen reduction activities in oxygen saturated condition. Onset potential for ORR can be observed at 0.96 V (vs RHE) in oxygen saturated CV studies. For hydrogen evolution

reaction (HER), onset potential is observed around 0 V (vs RHE). The polarization plot (Fig. S11b) displays excellent ORR performance of pPt-NTs. An enhancement in current density is observed with increase in the rotation rate applied to the sample from 225 to 2025 rpm. The reason for this is attributed to increased diffusion of oxygen molecules at electrode- electrolyte interface. The ORR performance of pPt-NTs is also compared with commercial Pt/C (Fig. S12a). It is observed that porous Pt nanotubes show comparable activity to commercial Pt/C in terms of onset potential (0.96V vs RHE) and current density (Refer Table 2). Very less (around 3%) formation of H_2O_2 is measured (Figures S11c and S12b&c). The electron transfer number is estimated to be around 4 during the reaction (Fig. S12b). Thus, we confirm that, pPt-NTs follow a direct pathway for the reduction of O_2 to H_2O, without involving a significant production of intermediate compounds.

The Koutecky-Levich (K-L) plots for pPt-NTs at different potentials from 0.45 V to 0.2 V (vs RHE) at different rotation rates (0 to 2025 rpm) are shown in Fig. S12d. The Levich current is directly proportional to the square root of the rate of rotation of the electrode. The linear region indicates first order kinetics for pPt-NTs. The slope of the curve drawn using K-L equation gives the number of electrons transferred during ORR. According to this electron transfer number is estimated to be around 4 giving a direct correlation with ‘n’ calculated from Eq. (2), which further confirms a direct pathway of reduction of O_2 to OH-.

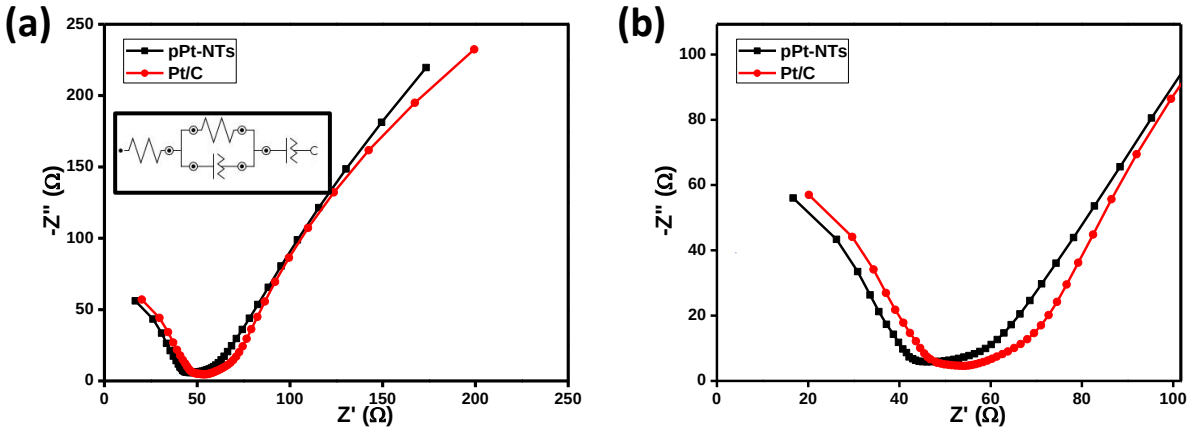

Fig. S13 (a) shows Electrochemical Impedance Spectroscopy of pPt-NTs vs commercial Pt/C at onset potential in alkaline medium along with the equivalent circuit diagram depicted on the inset (b) is the zoomed in image of the high frequency region.

Table 2: A comparison between pPt-NTs and commercial Pt/C, observed from Fig. S12a

	pPt-NTs	**Comm Pt/C**
Onset potential (V vs RHE)	0.95	0.99
Diffusion limited current density (mA/cm^2), observed at 0.4 V vs RHE	1.14	1.47
Half-wave potential ($E_{1/2}$; V vs RHE)	0.85	0.866
Mass activity (A g^{-1})	2.05	2.63

Sensing studies:

SO_2 gas sensing characteristics

The gas sensing studies were performed on these mesoporous ZPO nanotubes in a custom-constructed volumetric gas chamber connected to mass flow controllers (Alicat), SMU (Keithley 2450) and temperature controller (Eurotherm). To carry out the measurements, the fabrication of sensor device (Interdigitated electrodes) structure is performed by standard lift off process on a Si/SiO_2 substrate. The sensing film is coated on the active region of device structure using standard drop casting technique since these nanotubes were solution processed. The relative change in resistance/current is measured while the sensor is exposed to different analytes and the sensor response is determined by using the formula,

$$R(\%) = \frac{I_g - I_a}{I_a} x\ 100 \qquad (6)$$

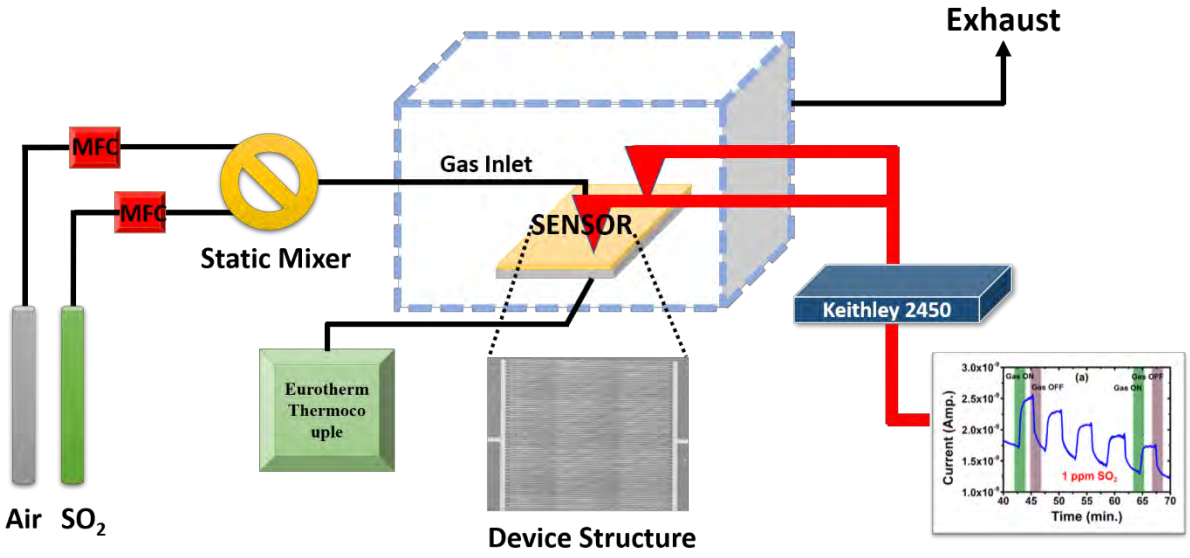

Fig. S14. Schematic of the gas sensing set up

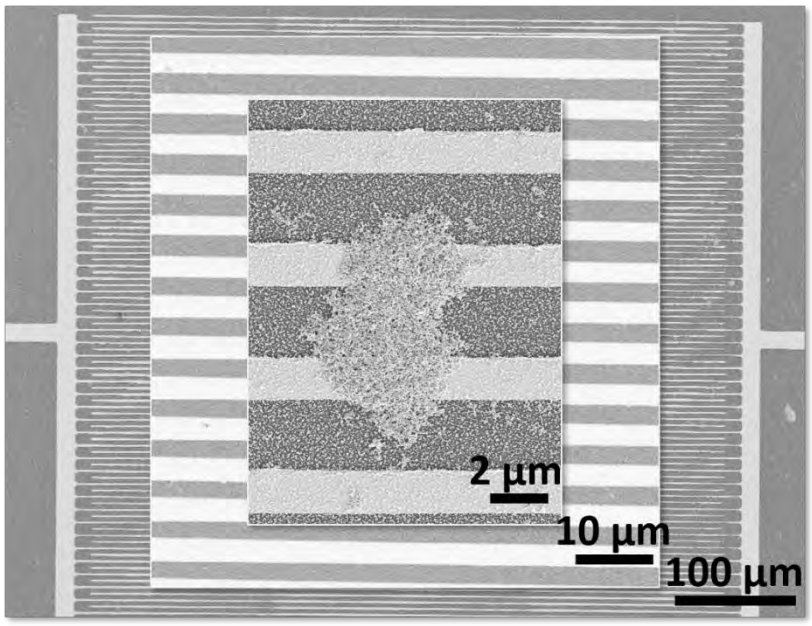

Fig. S15. SEM micrograph of Inter-digitated device structure with (magnified view)

The sensor memory effect is defined by formula,

$$\gamma Hy(\%) = \frac{\Delta I_{max}}{F_{fs}} \times 100 \qquad (7)$$

where ΔI_{max} represents algebraic difference between current values when the SO_2 concentration was raised from 0.3 ppm to 3 ppm and vice-versa, FFS is the full-scale output value defined as the highest current value observed with maximum input minus the one observed with minimum input (See, Fig. S16 b&c).

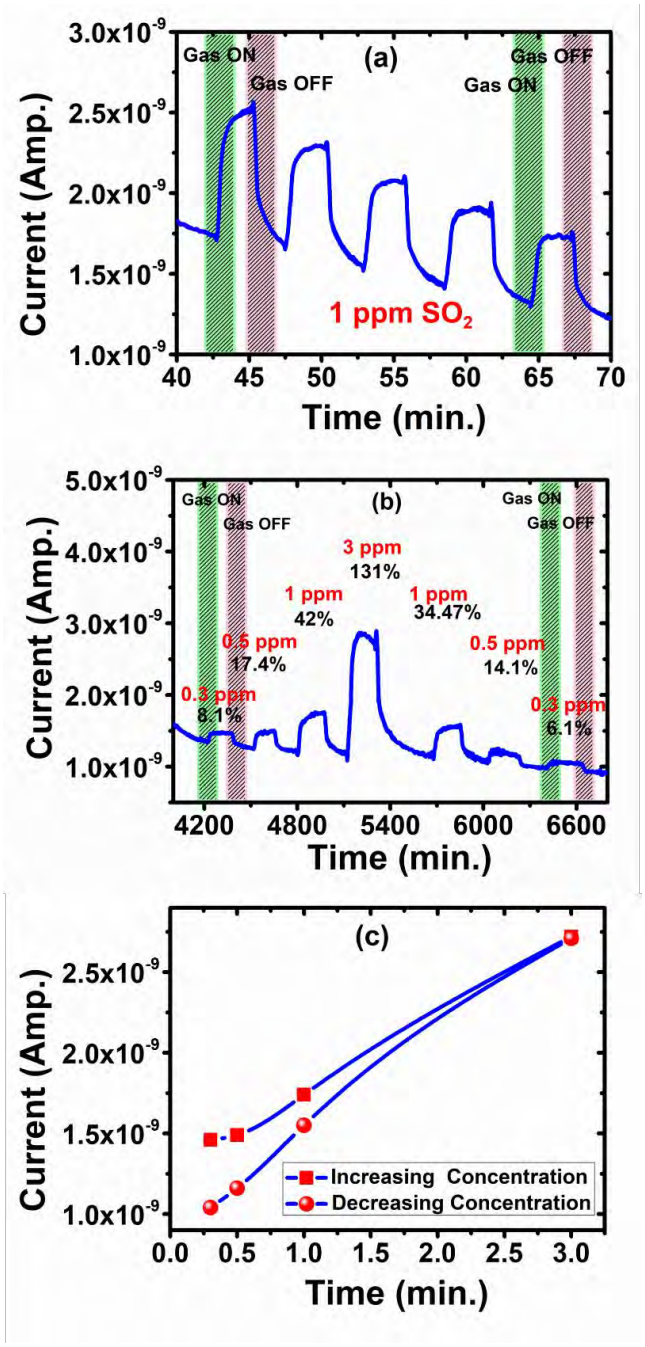

Fig. S16: (a) Transient sensing plot for five repeat cycles of 1 ppm SO_2, (b) Dynamic current variations while going from low to high concentration and vice-versa and (c) the associated hysteresis obtained from plot (b).

Table 3. Comparison of our work with existing reports in literature on SO_2 gas sensing

Material	Method	Response %	Temp (°C)	LOD	Res/Rec time (sec)	Ref
PANI nanostructures	Chemical Oxidative method	4.3%	RT	10 ppm	180s/220	[2]
PANI/WO_3	Chemical Oxidative method	4.3%	RT	5 ppm	180s/180	[3]
TiO_2/Graphene	Layer by layer Assembly	6.05%	RT	1 ppb	95s /128s	[4]
Au/ZnO	Sol-gel followed by precipitation	1%	RT	10 ppm	1500/3000	[5]
NiO/ZnO	Hydrothermal	16.25%	240	20 ppm	52/41	[6]
V_2O_5 thin film	Sputtering	0.7%	325	38 ppb	400/500	[7]
SnO_2 thin film	LASER ass. MOCVD	1%	268	1 ppm	300/---	[8]
Pt doped WO_3	RF Magnetron sputtering	5.9%	200	1 ppm	150/250	[9]
Zinc Platinate nanotubes	Microwave irradiation	8.1%	RT	300 ppb	7/9	(our work)

Gas Sensing Mechanism

A typical chemiresitive sensor works on the principle of charge transfer based on the adsorption of analyte gas molecules. The change in electrical conductivity is a measure of analyte adsorption on the surface of semiconductor metal oxides (SMOs'). Oxygen ion sorption at the surface mediates this charge transfer phenomenon. It is already understood well in literature that oxygen gets ionosorbed in different forms (O_2^-, O^-, O^{2-}) at different temperatures on the surface of SMO's as depicted in the reactions below[10].

$$O_2\,(ads) + e^- \rightarrow O_2^-\,(ads);\ T < 100^oC \quad (8)$$

$$O_2^-\,(ads) + e^- \rightarrow 2O^-(ads);\ 100 < T < 300\ ^oC \quad (9)$$

$$2O^-(ads) + e^- \rightarrow O^{2-}(ads);\ T > 300\ ^oC \quad (10)$$

Atmospheric oxygen adsorption on these mesoporous zinc palatinate nanotubes extracts electrons from the conduction band, resulting in the formation of a potential barrier near the surface. Consequently, the electron density decreases which lowers the electrical conductivity of the sensor material. As soon as SO_2 gas molecules interact with these nanotubes, it readily gets oxidized to SO_3 by reacting with ionosorbed oxygenated anionic species while releasing back the electron into the system. The release of electrons on the adsorption of SO_2 (a reducing

gas) indicates the n-type semiconducting behavior of zinc platinate nanotubes. The reaction kinematics is as follows:

$$2SO_2 + O_2^- (ads) \rightarrow 2SO_3 + e^- \quad (11)$$

Furthermore, the mesoporous nature of these nanotubes adds to the enhancement of surface area and hence the sensitivity. As confirmed by BET measurements, the surface area is computed to be 54 m^2/g. The porosity and enlarged surface area introduce numerous active sites of adsorption by allowing the gas to diffuse to the inner regions of these hollow tubes. The swift response observed in the interaction of SO_2 can be attributed to the porous nature of these nanotubes. Therefore, it can be concluded that this 1D hollow nanotubular structure of zinc platinate plays an important role in enhancing the overall metrics of the sensor.

References

1 N. Sakhuja, R. K. Jha, R. Chaurasiya, A. Dixit and N. Bhat, *ACS Appl. Nano Mater.*, 2020, **3**, 3382–3394.

2 V. Chaudhary and A. Kaur, *Polym. Int.*, 2015, **64**, 1475–1481.

3 V. Chaudhary and A. Kaur, *RSC Adv.*, 2015, **5**, 73535–73544.

4 D. Zhang, J. Liu, C. Jiang, P. Li and Y. Sun, *Sensors Actuators, B Chem.*, 2017, **245**, 560–567.

5 A. Gaiardo, B. Fabbri, A. Giberti, V. Guidi, P. Bellutti, C. Malagù, M. Valt, G. Pepponi, S. Gherardi, G. Zonta, A. Martucci, M. Sturaro and N. Landini, *Sensors Actuators, B Chem.*, 2016, **237**, 1085–1094.

6 Q. Zhou, W. Zeng, W. Chen, L. Xu, R. Kumar and A. Umar, *Sensors Actuators, B Chem.*, 2019, **298**, 126870.

7 C. S. Prajapati and N. Bhat, *Proc. IEEE Sensors*, 2018, **2018-Octob**, 1–4.

8 J. Lančok, A. Santoni, M. Penza, S. Loreti, I. Menicucci, C. Minarini and M. Jelinek, *Surf. Coatings Technol.*, 2005, **200**, 1057–1060.

9 M. Stankova, X. Vilanova, J. Calderer, E. Llobet, P. Ivanov, I. Grácia, C. Cané and X. Correig, *Sensors Actuators, B Chem.*, 2004, **102**, 219–225.

10 A. Dey, *Mater. Sci. Eng. B*, 2018, **229**, 206–217.